

Dark Matter Search with a Resonantly-Coupled Hybrid Spin System

Kai Wei,^{1,2,3,*} Zitong Xu,^{4,1,2,*} Yuxuan He,⁵ Xiaolin Ma,⁵ Xing Heng,^{1,2} Xiaofei Huang,^{1,2} Wei Quan,^{1,2} Wei Ji,^{5,6,7,†} Jia Liu,^{5,8,‡} Xiao-Ping Wang,^{9,10} Dmitry Budker,^{6,7,11} and Jiancheng Fang^{1,2,3,§}

¹*School of Instrumentation Science and Opto-electronics Engineering, Beihang University, Beijing, 100191, China*

²*Hangzhou Extremely Weak Magnetic Field Major Science and Technology Infrastructure Research Institute, Hangzhou, 310051, China*

³*Hefei National Laboratory, Hefei 230088, China*

⁴*School of Physical and Mathematical Sciences, Nanyang Technological University, Singapore, 639798, Singapore*

⁵*School of Physics and State Key Laboratory of Nuclear Physics and Technology, Peking University, Beijing 100871, China*

⁶*Johannes Gutenberg University, Mainz 55128, Germany*

⁷*Helmholtz-Institute, GSI Helmholtzzentrum für Schwerionenforschung, Mainz 55128, Germany*

⁸*Center for High Energy Physics, Peking University, Beijing 100871, China*

⁹*School of Physics, Beihang University, Beijing 100191, China*

¹⁰*Beijing Key Laboratory of Advanced Nuclear Materials and Physics, Beihang University, Beijing 100191, China*

¹¹*Department of Physics, University of California at Berkeley, Berkeley, California 94720-7300, USA*

Recent advances in tabletop quantum sensor technology have enabled searches for nongravitational interactions of dark matter (DM). Traditional axion DM experiments rely on sharp resonance, resulting in extensive scanning time to cover a wide mass range. In this work, we present a broadband approach in an alkali-²¹Ne spin system. We identify two distinct hybrid spin-coupled regimes: a self-compensation (SC) regime at low frequencies and a hybrid spin resonance (HSR) regime at higher frequencies. By utilizing these two distinct regimes, we significantly enhance the bandwidth of ²¹Ne nuclear spin compared to conventional nuclear magnetic resonance, while maintaining competitive sensitivity. We present a comprehensive broadband search for axion-like dark matter, covering 5 orders of magnitude of Compton frequencies range within $[10^{-2}, 10^3]$ Hz. We set new constraints on the axion dark matter interactions with neutrons and protons, accounting for the effects of DM stochasticity. For the axion-neutron coupling, our results reach a low value of $|g_{ann}| \leq 3 \times 10^{-10}$ in the frequency range $[2 \times 10^{-2}, 4]$ Hz surpassing astrophysical limits and providing the strongest laboratory constraints in the $[10, 100]$ Hz range. For the axion-proton coupling, we offer the best terrestrial constraints for the frequency ranges $[2 \times 10^{-2}, 5]$ Hz and $[16, 7 \times 10^2]$ Hz.

Introduction

There is evidence of dark matter (DM) from numerous astrophysical and cosmological observations. However, its nature is yet to be understood, which is one of the most important challenges in modern physics. Ultralight pseudoscalar particles, such as axions or axionlike particles (ALPs) [1, 2], are well-motivated dark matter candidates, which can be produced via the “misalignment mechanism” to obtain the correct relic abundance [3–7]. The axion is particularly well motivated as it also solves the so-called strong-CP problem by introducing the Peccei-Quinn global symmetry [8–11]. It (weakly) couples to other particles [12] due to the spontaneous breaking at high energy, making it difficult to detect in experiments. In this article, we refer to both axions and ALPs as “axions”, so that the coupling to photons, gluons and fermions can span a wide range of parameter space which has been explored in various astrophysical and laboratory experiments [13–15].

Regarding the coupling to nucleons, the axion gradient field can be measured as a pseudomagnetic field coupling to the nuclei. In the non-relativistic limit, the gradient interaction can be described by the Hamiltonian,

$$\mathcal{H} = g_{aNN} \nabla \mathbf{a} \cdot \mathbf{I}, \quad (1)$$

where \mathbf{I} is the spin of the nucleus which includes fraction of spins of the neutron and proton, and g_{aNN} is the effective axion coupling to the nucleus. Therefore, the pseudomagnetic field due to the axion DM is $\mathbf{b}_a \equiv g_{aNN} \nabla \mathbf{a} / \gamma_n$, where γ_n is the

gyromagnetic ratio of the nuclear spin.

Recent experiments are using various nuclei, including the liquid state experiments using proton and ¹³C [16] and gas state sensors based on alkali-noble pairs using ³He [17–19] and ¹²⁹Xe [20]. These terrestrial experiments explore the nuclear precession frequency range from μ Hz to hundreds of kHz, corresponding to the axion mass range from 10^{-22} to 10^{-10} eV. In the frequency range from approximately 0.01 Hz to 10 Hz, the ³He comagnetometer [18], together with our previous work through the ChangE collaboration (Coupled Hot Atom eNsembles for liGht dark mattEr) on the bandwidth-enhanced nuclear magnetic resonance (NMR) magnetometer [21] sets limits on the axion-neutron coupling to be lower than 10^{-9} GeV^{-1} . A recent ³He comagnetometer [19] provides slightly weaker limits in the 0.01 Hz to 10 Hz range but can extend these limits down to $\mathcal{O}(10^{-7})$ Hz frequencies.

Typically, to expand the search range for DM with gas-state quantum sensors, a bias magnetic field is applied. The resonance frequency is scanned by adjusting the external magnetic field to match the Larmor frequency with the axion Compton frequency. In [17], a spin-exchange-relaxation-free (SERF) magnetometer used with a leading field that is sufficiently high to break the SERF regime, leading to increased spin-exchange relaxation. In [20], a spin-based amplifier is applied, where the resonance frequency is scanned by adjusting the external magnetic field to match the Larmor frequency with the axion Compton frequency. Resonant searches benefit from high Q factors at the resonant frequency but suffer from

narrow bandwidth, typically at the level of 0.01 Hz for Xe [20] and Ne [21]. Thus, to search for an axion with unknown mass, one needs to scan the frequency with steps corresponding to the narrow bandwidth to cover the target frequency range, rendering resonant searches to be time-consuming.

In this work, we apply the hybrid spin manipulation method, first proposed and demonstrated in the K- ^3He system [22], to conduct a broadband search using the K-Rb- ^{21}Ne system. In ^{21}Ne system, we identify two distinct regimes: one resembling the self-compensation (SC) regime observed in the ^3He system, and another at a higher frequency which we term as the hybrid spin resonance (HSR) mode. The SC and HSR regimes for the K- ^3He system are nearly degenerate, limiting the bandwidth coverage in the dark matter search. These regimes exhibit a significantly broader bandwidth compared to typical NMR magnetometers, while maintaining competitive sensitivity in both cases. They allow for the transformation of the conventional narrow-band resonant search into a broadband search for axion dark matter, benefiting from extended experiment durations. We utilize the K-Rb- ^{21}Ne sensor to search for axion dark matter spanning 5 orders of magnitude, [0.01, 1000] Hz in the frequency range. After analyzing the data and rigorously examining potential candidates, we establish new constraints on the axion-neutron and axion-proton couplings.

RESULTS

Experimental Setup

We use a K-Rb- ^{21}Ne hybrid thermal spin ensembles in which the minority potassium atoms are used for “hybrid optical pumping” [23] and the mixed spin ensemble of alkali metal and noble gas is operated in a regime where the two spin species are resonantly-coupled and under the influence of the magnetic field from each other. The alkali metal gas and noble gas undergo hybrid spin resonance under an appropriate external magnetic field.

The experimental setup comprises a spherical cell with a 11.4 mm internal diameter that holds a small droplet of K and Rb metal, along with 70% isotope-enriched ^{21}Ne . To prevent the spontaneous emission transition of alkali atoms in the excited state and the generation of resonant photons with random spin polarization, we used N_2 gas as a quenching gas. The alkali atoms are spin-polarized with circularly-polarized light tuned to the potassium D1 line. The hybrid optical pumping is used to improve the hyperpolarization efficiency for ^{21}Ne nuclear spins and reduce the polarization gradient of alkali spins, which is achieved by optically pumping the optically-thin potassium vapor to avoid strong resonant absorption of the pump light [24, 25]. The spin angular momentum is transferred from the “minority” K atoms to the Rb atoms and the ^{21}Ne nuclear spins via spin-exchange collisions. Additionally, ^{21}Ne gas also acts as a buffer gas to reduce the rapid wall-collision relaxation of alkali spins. The precession of polarized ^{21}Ne nuclear spins is monitored with optically-thick Rb spins, read out by detecting optical rotation of linearly-polarized probe light detuned to low-frequency

side of the D1 line of Rb. The above processes can be summarized as an illustration picture in Fig. 1.

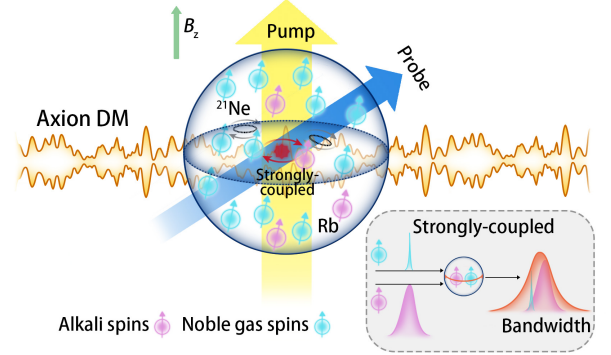


FIG. 1. The principle of HSR and dark matter detection: (1) Pump light polarizes the alkali electron spins, while spin-exchange collisions with alkali spins polarize the noble-gas nuclear spins. (2) The axion dark matter produced a pseudomagnetic field acting on nuclear spins. The precession of nuclear spins is transferred to alkali spins via Fermi-contact interactions. (3) The resulting precession of the alkali spins is read out using optical rotation of the probe light. Normally, the measurement bandwidth of noble-gas nuclear spins is narrow due to their small relaxation rate Γ_n (blue peak), which is several orders of magnitude smaller than that of alkali spins (purple peak). However, in the HSR regime, the noble-gas spins become resonantly-coupled with alkali spins. As a result, the interactions with alkali spins significantly broaden the bandwidth of the noble-gas spins (red peak).

Hybrid Spin Dynamics

The spin interactions between hyperpolarized ^{21}Ne atoms and spin-polarized alkali atoms are dominated by Fermi-contact interactions (FCI), which can be characterized as effective fields $\mathbf{B}^{e/n} = \lambda M_0^{e/n} \mathbf{P}^{e/n}$ due to the magnetization of the other spin species, where λ is the Fermi-contact enhancement factor, $M_0^{e/n}$ is magnetization of alkali (noble-gas) atoms for fully polarization, $\mathbf{P}^{e/n}$ is the collective spin polarization of alkali (noble-gas) spin ensembles. Therefore, the total fields experienced by alkali spins and noble-gas spins are $\mathbf{B}_{\text{tot}}^e = \mathbf{B}^n + \mathbf{B}$ and $\mathbf{B}_{\text{tot}}^n = \mathbf{B}^e + \mathbf{B}$ respectively, where \mathbf{B} is the applied magnetic field. Typically, the gyromagnetic ratio of alkali spins is much larger than that of noble-gas nuclear spins. Consequently, the Larmor frequency of alkali spins at a given field is usually orders of magnitude higher than that of noble-gas spins.

The dynamics of the spins can be characterized to two special regimes which have unique features. One is the SC regime, where we adjust the external magnetic field to $B_{\text{SC}} = -B_z^n - B_z^e$, which corresponds to approximately 576.2 nT in Fig. 2. As a result, it cancels the effective magnetic field from noble gas \mathbf{B}^n , and the slow changes in the magnetic field are automatically canceled by interactions between the alkali and noble-gas atoms [22, 25].

The second regime occurs when the external magnetic field

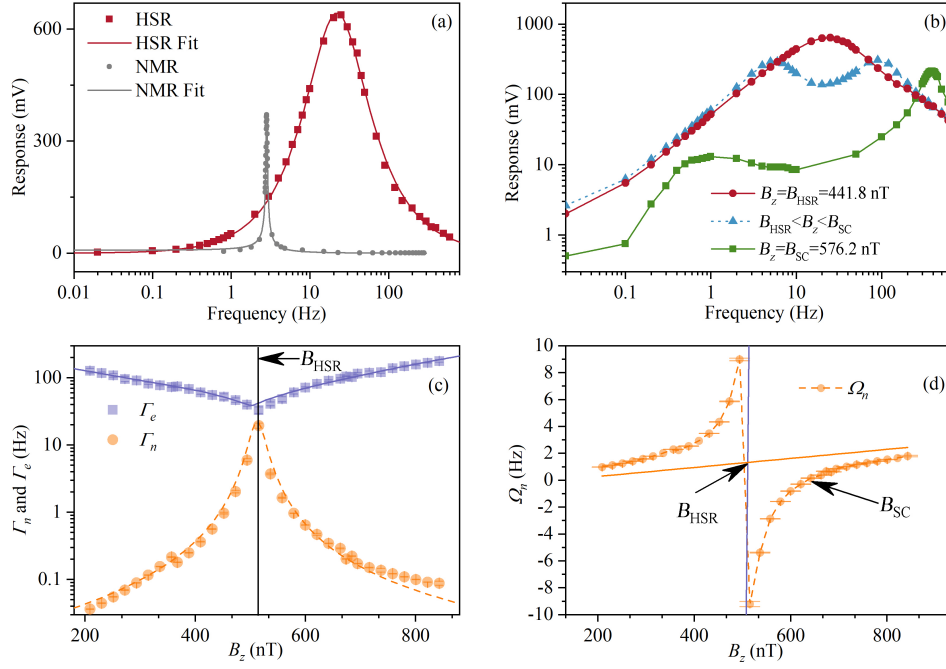


FIG. 2. Proof-of-principle demonstration of a resonantly-coupled hybrid spin resonance. (a) The response comparison of the HSR and NMR regimes. (b) Responses to an oscillating magnetic field applied along \hat{x} as a function of the oscillation frequency for three different working regimes: the SC regime with the external magnetic field $B_z = B_{SC} = 576.2$ nT, the HSR regime with $B_z = B_{HSR} = 441.8$ nT, and an intermediate regime between the two with $B_z = 459.3$ nT. In (a) and (b), the comparisons are under the same conditions except for different B_z values. (c) The relaxation rates of the transverse spin components of alkali spins Γ_e and noble-gas spins, Γ_n , as a function of B_z . (d) The precession frequency Ω_n of noble-gas nuclear spins as a function of the bias field.

B_z is tuned to $B_{HSR} \simeq -B_z^n$, which corresponds to approximately 441.8 nT in Fig. 2. Due to the screening effect of the noble gas field, the alkali atoms experience a much smaller magnetic field and precess slowly to match the precession frequency of the noble gas atoms. We term as HSR to show this merit. Due to the hybrid resonance and strong Fermi-contact interaction, the alkali and noble-gas spins become resonantly-coupled. The damping rate of alkali spins is slowed by the noble-gas spins, while the noble-gas spin damping is accelerated by the alkali spins, similar to the fast-damping effect seen in the ^3He system [22, 26]. Consequently, the bandwidth of the noble-gas nuclear spins is significantly enhanced compared to typical NMR mode. In addition, the central frequency of the ^{21}Ne HSR is more than an order of magnitude higher than that of the SC regime (see detailed explanations for Fig. 2(b)).

Both SC and HSR regimes have been demonstrated in Ref. [22, 27] using the K- ^3He system. Besides, Ref. [26] also studied a strong coupling dynamics of K- ^3He for periodic exchange of the two spins. However, because the effective field from K atoms B_z^e is too weak, which is more than two orders of magnitude smaller than that of B_z^n , these two regimes are nearly degenerate and cannot be well separated for the purpose of enhancing the bandwidth of the system. In the K-Rb- ^{21}Ne system demonstrated here, the B_z^e is more than two orders of magnitude larger than that of K- ^3He system, due to its stronger Fermi-contact enhancement factor and a higher

alkali atom density. This enabled us to detect low frequency dark matter with enhanced sensitivity via the SC regime and to detect high frequency dark matter with enhanced bandwidth by the HSR mode.

A detailed description of the SC mode can be found in [25], and we now describe the key features of the HSR regime in the ^{21}Ne system. We experimentally demonstrate the HSR regime as shown in Fig. 2. The responses of the alkali-noble-gas spins to an oscillating magnetic field are shown in Fig. 2(a) for the traditional NMR regime (gray) and the HSR regime (red). In the NMR case, the bandwidth is approximately 0.01 Hz, which is the typical bandwidth of NMR spin magnetometers [20, 21]. By operating the noble-gas and alkali spin ensembles in the HSR regime, the response to the magnetic field is broadened to a full-width half-maximum (FWHM) bandwidth of 36.65 Hz centering around 21.99 Hz, which represent three orders of magnitude improvement compared with that of the NMR regime [20].

In Fig. 2(b), when setting the bias field B_z to the SC point B_{SC} (green), there are two separate peaks in the frequency response. The low-frequency peak originates from noble-gas nuclear spins, while the high-frequency peak is from alkali spins. For the bias field B_z between the SC point B_{SC} and the HSR point B_{HSR} (blue), the response peaks of noble-gas nuclear spins and alkali spins move closer together. Finally, when the bias field is set to the HSR point B_{HSR} (red), the two peaks merge and form a broadened HSR peak. The cen-

tral peak frequencies of the ^{21}Ne system in the HSR and SC regimes are approximately 22 Hz and approximately 0.9 Hz, respectively, separated by more than an order of magnitude, which is a clear distinction from the ^3He system.

To present the changes in bandwidth of alkali spins and noble-gas spins, we measure the relaxation rate (damping rate) of the transverse spin component of two spin species respectively. As shown in Fig. 2(c), the damping rate Γ_e of alkali electron spins decreases as the bias field B_z approaches the HSR point B_{HSR} , while the damping rate Γ_n of noble-gas nuclear spins increases from approximately 0.04 Hz to about 20 Hz. This result intuitively presents that the relaxation rate of the alkali electron spins is slowed down by resonant coupling with noble-gas nuclear spins, while the noble-gas nuclear spins are sped up. Therefore, the hybrid response peak is no longer contributed by two spin species separately. Rather, the peak is due to the resonantly-coupled hybrid spin ensembles. The bandwidth of the HSR is a hybrid combination of Γ_e , Γ_n , B_z^e , and B_z^n , and also depends on the bias field B_z (see Materials and Methods).

As shown in Fig. 2(d), when working away from the HSR point, the noble-gas precession frequency Ω_n gradually approaches the asymptotic frequency (orange solid line) $\Omega_n = \gamma_n(B_z + B_z^e)$, which is the Larmor precession of uncoupled noble-gas spins. However, when working around the HSR point, the noble-gas's precession rate approaches the asymptotic frequency (purple solid line) $\Omega_e = \gamma_e(B_z + B_z^n)$, which is the precession frequency of uncoupled alkali atoms. In this region, because of the resonant coupling between alkali and noble gas atoms, the precession of noble-gas is dominated by the alkali atoms, and its precession frequency reaches the maximum. The hybrid responses of two types of atomic spins provide a new way to manipulate the gyromagnetic ratio of different atoms.

Experimental Sensitivity

We now discuss the magnetic and dark-matter sensitivity of the HSR regime. The sensitivity of the setup is calibrated by applying oscillating magnetic fields generated with a magnetic coil. The spectrum of the setup, shown in Fig. 3, demonstrates a sensitivity of $0.78 \text{ fT/Hz}^{1/2}$ from 28 to 32 Hz, which is remarkably high for comagnetometers. The magnetic noise of the inner Mn-Zn ferrite shield in the relevant frequency range is estimated to be $2.5 f^{-1/2} \text{ fT}$ (f is the frequency in Hz) [28], using the measured relative permeability and geometrical parameters of the shield. Details about vibration and magnetic noise can be found in the supplementary information in Ref. [24]. This means that the estimated magnetic noise from the shield is close to the total noise level. The background noise of the probe with pump light blocked is about $0.2 \text{ fT/Hz}^{1/2}$ from 28 to 32 Hz, which is significantly smaller than the total noise. The spin-projection noise of alkali spins is calculated to be about $0.09 \text{ fT/Hz}^{1/2}$ [29].

In HSR regime, the relationship between the response to ultralight dark matter field b_x^n coupling with noble-gas nuclear spins $S_x^e = K_{b_x^n} b_x^n$ and the response to magnetic field

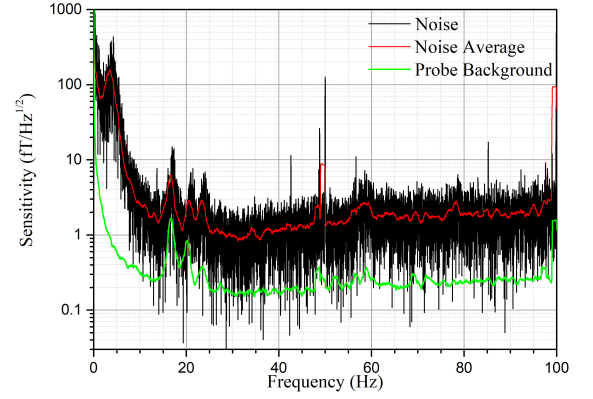


FIG. 3. The sensitivity at the hybrid spin resonance to a \hat{y} -directed magnetic field is $0.78 \text{ fT/Hz}^{1/2}$ from 28 to 32 Hz, placing the system among the most sensitive sensors using alkali-metal spins to measure the precession of noble-gas nuclear spins. The noise peaks around 6 Hz, and from 17 to 23 Hz are due to the vibrations, which is verified with a seismometer. The noise peak at 50 Hz is the power-line noise. The background noise of the probe with pump light blocked is much smaller than the total noise level.

$S_x^e = K_{B_y} B_y$ is derived in Materials and Methods in details. The two response factors are related as,

$$K_{B_y} = K_{b_x^n} \omega / \omega_z^n, \quad (2)$$

where $\omega_z^n = \gamma_n B_z^n$ and ω is the angular frequency of the signal b_x^n . Therefore, we can use the normal magnetic field to calibrate the response to the pseudomagnetic field b_x^n .

Axion Dark Matter Searches

The gradient axion field can couple with the nucleon magnetic dipole moment and can be viewed as a pseudomagnetic field, \mathbf{b}_a . By measuring its effects on the nuclear spins, separate from the normal magnetic field, we can identify its existence and constrain its magnitude. The gradient of the axion dark matter field in a volume V can be written as

$$\nabla a(x) = \sum_{\mathbf{p}} \sqrt{\frac{2N_{\mathbf{p}}}{V\omega_{\mathbf{p}}}} \cos(\omega_{\mathbf{p}}t - \mathbf{p} \cdot \mathbf{x} + \phi_{\mathbf{p}}) \mathbf{p}, \quad (3)$$

where the sum runs over all momentum modes \mathbf{p} , $\phi_{\mathbf{p}}$ is the random initial phase related to the mode \mathbf{p} modeled as a uniform variable in the $[0, 2\pi]$ interval, $N_{\mathbf{p}} = \rho_{\text{DM}} V f(\mathbf{p}) (\Delta p)^3 / \omega_{\mathbf{p}}$ is the mean occupation number of mode \mathbf{p} . The function $f(\mathbf{p})$ is the Maxwell-Boltzmann velocity distribution for DM in the Standard Halo Model [30] and is normalized to $\int d\mathbf{p} f(\mathbf{p}) = 1$, and $\rho_{\text{DM}} = 0.4 \text{ GeV} \cdot \text{cm}^{-3}$ is an estimate of local DM energy density [31]. Possibilities of local enhancement of both the density and coherence time of the dark matter field have been considered (see, for example, [32]). Nevertheless, we present our analysis based on the Standard Halo Model.

The sum over all \mathbf{p} modes leads to a stochastic pattern [18, 33–36], which can be noticed for an experiment duration longer than the characteristic coherence time $\tau_a \approx m_a^{-1} \sigma_v^{-2} \hbar$ [37] with the DM velocity dispersion $\sigma_v =$

$220/\sqrt{2} \text{ km} \cdot \text{s}^{-1}$. We account for the DM stochastic effects in the analysis following the frequency-domain likelihood-based formalism of Ref. [18].

For high-frequency measurements, we conducted a 209-hour measurement with an 86% duty cycle (Dataset 1) and a 4-hour continuous measurement with a nearly identical setup deployed in an underground laboratory (Dataset 2), which provided better suppression of vibrations and power-line interference. Both measurements were conducted at a fixed bias magnetic field in the HSR regime. For low-frequency measurements, we employed the SC regime and collected 146 hours of data (Dataset 3). We used the log-likelihood ratio (LLR) test to analyze the datasets, obtain exclusion limits for the magnitude of the pseudomagnetic field, and convert these to limits for axion-nucleon couplings. The calculations closely follow those in Ref. [18], with details provided in Materials and Methods.

In Fig. 4, we set exclusion limits (95% C.L.) in red for axion-neutron g_{ann} and axion-proton g_{app} couplings. For the axion-neutron coupling g_{ann} , the HSR limits reach down to $\mathcal{O}(3 \times 10^{-9} \text{ GeV}^{-1})$, close to the astrophysics limits and improve on the results from NASDUCK-Floquet [39] by 1-2 orders of magnitude. Note that the work [20] also reported a series of “needle” exclusions in the frequency range of 1 Hz to 200 Hz with a typical width of 35.8 mHz. When comparing these results, it is essential to consider the stochastic correction and the neutron polarization correction, ξ_n in ^{129}Xe . In order to attain continuous exclusion, the study presented in [20] necessitates an accumulation period of about 3 years, while our data takes a significantly shorter duration of just one week. The SC limits are comparable to the $\text{K-}^3\text{He}$ results [18], while providing slightly better constraints for the frequency range of $[2 \times 10^{-2}, 2 \times 10^{-1}] \text{ Hz}$. This improved sensitivity is due to the smaller gyromagnetic ratio of ^{21}Ne compared to ^3He , despite the shorter measurement time 146 hr comparing with the 40-day duration of $\text{K-}^3\text{He}$ results [18]. Our results show slightly weaker sensitivity in the frequency range of 4.5 to 15.5 Hz compared to our previous bandwidth-enhanced NMR magnetometer work [21], but they cover a significantly larger bandwidth in terms of axion mass. Our laboratory limits for g_{ann} are stronger than the astrophysical limits based on the emission of neutron stars [41] and supernova SN1987A [42] for low f_a and are comparable at intermediate frequencies $\sim \mathcal{O}(10) \text{ Hz}$. It is important to note that astrophysical limits are subject to various uncertainties, such as density-dependent coupling, unknown heating mechanisms for neutron stars [41, 44, 45], and axion production, scattering, and absorption in dense plasma environments, as well as the model dependence of the collapse mechanism for supernovae [42, 46, 47].

For the axion-proton coupling g_{app} , we have achieved the most stringent terrestrial constraints across an extensive frequency range of $[2 \times 10^{-2}, 5] \text{ Hz}$ and $[16, 7 \times 10^2] \text{ Hz}$ using the SC and HSR data, complementary to our previous enhanced NMR experiment [21]. In principle, the proton’s fraction of spin in ^3He can be taken into account, then the $\text{K-}^3\text{He}$

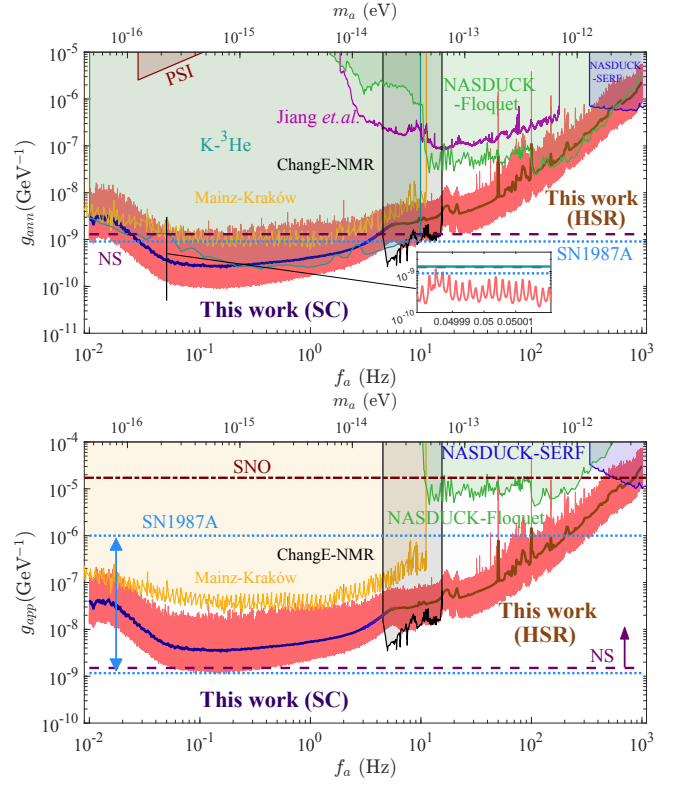


FIG. 4. The 95% C.L. upper limits on the axion-neutron coupling g_{ann} and axion-proton coupling g_{app} from both the SC and HSR measurements are shown as red lines. The full data of the limits cannot be shown in the figure, but are tabulated in [38]. To guide the readers’ eye, for each f_a , the couplings g_{ann} and g_{app} are averaged in a bin from $0.99f_a$ to $1.01f_a$, following [39]. The averaged limits are shown in dark blue for SC data (labeled as “This work (SC)”, covering the range $[0.01, 6] \text{ Hz}$) and in brown for HSR data (labeled as “This work (HSR)”, covering the range $[3, 1000] \text{ Hz}$). For the $[3, 6] \text{ Hz}$ range, we choose the stronger limits from the SC and HSR results. We also show other terrestrial limits from our previous results with bandwidth-enhanced NMR experiment [21] (ChangE-NMR) as well as that of Jiang et al. [20] with a conversion from nucleus coupling to nucleon coupling implemented, $\text{K-}^3\text{He}$ comagnetometer [18], NASDUCK-Floquet [39], NASDUCK-SERF [17], Mainz-Kraków [19], CASPER-ZULF [16] and PSI [40]. The astrophysical limits from neutron star (NS) cooling [41], supernova SN1987A [42] and solar axion at SNO [43] are shown as horizontal lines respectively.

system can also provide a strong limit on g_{app} in the corresponding frequency range. In Fig. 4, we compared our results with previous results. The precise proton fraction ξ_p^{Xe} within the Xenon nuclear spin is associated with unbounded uncertainties [39]. Therefore, we select the conservative result among the four models presented in NASDUCK-Floquet [39].

Aside from setting limits on axion couplings, a post-analysis is carried out (see Materials and Methods) to test the significance of the best-fit signal compared to the background-only model and to statistically assess any data points that exceed the 5σ threshold. With the look-elsewhere effect taken into account, we use $\text{LLR} > 52.1$ for a one-sided

global significance of a 5σ test [18]. Combining the two HSR data sets, we found that only 62 out of 6.8 million tested axion masses surpassed the 5σ confidence level, a small fraction of the total data set. No further $\geq 5\sigma$ candidates were identified in Dataset 3 (SC). This indicates that the majority of the data are consistent with the white noise background assumption. Nonetheless, a few peaks “survived” and it is possible that they could originate from axion DM. Consequently, we subjected the 62 candidates to three additional tests, as detailed in Materials and Methods, which led to the exclusion of these candidates as being a dark matter origin. Note that the other results, for example NASDUCK-SERF [17] have also seen numerous ‘candidate’ peaks in the data that are likely due to systematic effects. Though, the candidate at a frequency of $f_a = 46.704996$ Hz is marginally excluded at the 95% confidence level. We emphasize that quantitative exclusions may be less reliable due to the potential violation of the white noise assumption resulting from the presence of systematic noises. It would be useful to revisit these points in future studies where spurious peaks may arise at different locations with independent setups, thus these regions can be covered.

DISCUSSION

We demonstrate a new HSR regime that can be used for a broadband search for new physics such as dark matter. The embedded alkali SERF magnetometer enables high sensitivity to magnetic fields, and the HSR coupling broadens the bandwidth. This work paves a way to enhance the bandwidth and the sensitivity simultaneously, contrary to those improving the bandwidth at the cost of sensitivity degradation. We operated the alkali-noble-gas spin ensembles in SC and HSR working regimes, searching for dark matter in the frequency range from 0.01 Hz to 1 kHz. We found a number of candidates but rejected them based on their non-compliance with the expected properties of DM signals. We obtained limits that surpass previous laboratory results and, within a certain axion mass range, even exceed those from astrophysics with strong model assumptions. In addition, for the axion-proton coupling g_{app} , we achieved the most stringent terrestrial constraints for the frequency range $[2 \times 10^{-2}, 5]$ Hz and $[16, 7 \times 10^2]$ Hz.

The current dominant source of noise is magnetic noise from the shielding material. To improve the performance of the comagnetometer, additional active magnetic noise compensation loops can be utilized. Using better shielding material (for example, superconducting) or a bigger shielded room can also help since magnetic noise reduces with the shield size. In scenarios requiring the measurement of low-frequency signals, such as low-frequency dark matter detection and inertial rotation measurements, the SC mode can be utilized due to its effective suppression of low-frequency magnetic noise. Further improvements can be achieved by reducing the effective magnetic field gradient and enhancing the effective magnetic field from nuclear spins, thereby increasing the noise suppression capability of the SC mode. In future work, the HSR/SC magnetometer can be utilized

to search for new physics including exotic spin-dependent forces [24]. A network of HSR/SC magnetometers can be applied to search for topological defect dark matter [48], and can work in the intensity interferometry mode to detect dark matter in a much higher frequency range above the magnetometer bandwidth [49]. The broadband search can also be applied in other fields that need high bandwidth and ultrahigh sensitivity, for instance the measurement of brain signal for magnetoencephalogram [50], as well as the measurement of magnetism of ancient rocks to study global climate change history [51].

MATERIALS AND METHODS

Detailed Experimental Configurations

The experimental setup is demonstrated in Fig. 5. Within a 11.4 mm diameter spherical cell, a small droplet of K and Rb alkali metal atoms is combined with about 3 amg ^{21}Ne (70% isotope enriched) and 0.066 amg N_2 . The density ratio of K to Rb is set to approximately 1/55 to enhance polarization efficiency, improve uniformity, and increase sensitivity [23, 25, 52].

To fabricate a hybrid alkali-metal cell with a designed density ratio, a specialized process is required beyond standard cell preparation. First, the alkali-metal mixture is carefully weighed in an anaerobic environment to maintain the desired ratio. Next, the mixture is connected to a gas chamber fabrication device. It is introduced into the gas chamber using a controlled flame-sealing technique. Finally, after the glass cell is sintered down, careful testing of density ratio and selection of glass cell are necessary.

To maintain a stable temperature while reducing noise, the cell is heated to around 473 K using electric heaters. The AC electric heater is located inside a PEEK vacuum chamber with water-cooling. This design reduces heat dissipation and minimizes the impact of air convection on the pump and probe lights. Additionally, the water-cooled chamber helps lower the temperature of surrounding magnetic shields, thereby improving the magnetic noise performance. The current through the heaters is modulated at a high frequency of 200 kHz to minimize low-frequency magnetic noise from heating. In addition, a double-layer printed heating coil is employed to cancel out the magnetic noise from each heating coil. A homemade heating closed-loop control system ensures temperature stability.

The atomic cell is enclosed in a ferrite shield and a five-layer μ -metal magnetic shield to provide an ultralow magnetic noise condition. The magnetic noise of ferrite shield itself is optimized by comparing the performance of different material composition. The optimized ferrite shield features a low intrinsic magnetic noise at the level of $\text{sub-fT/Hz}^{1/2}$. Inside the ferrite shield, three-axis coils wrapped around the vacuum chamber further reduce the residual magnetic field due to the shield and facilitate spin ensemble manipulation.

Hybrid spin-exchange optical pumping is employed. A circularly polarized pump light along the z -axis is locked to the D1-line frequency of K atoms and utilized to polarize the

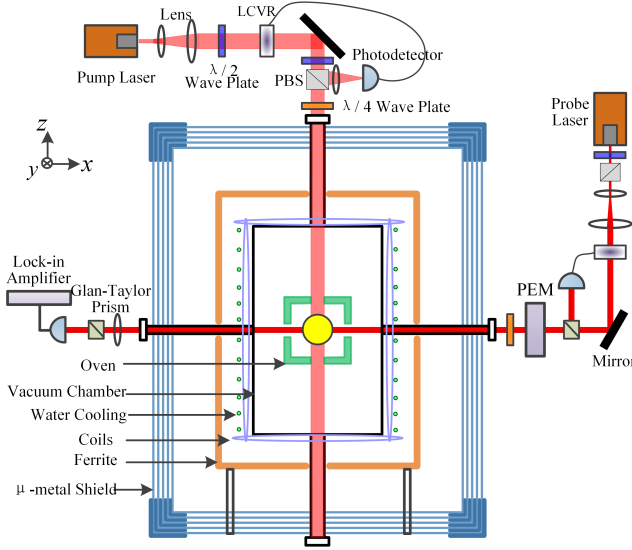


FIG. 5. The illustration of the experiment setup. At the center of the device is a glass cell containing a droplet of mixed K-Rb alkali metal, 3 amg ^{21}Ne , 0.066 amg N_2 , is installed in an oven, which is heated with an AC electric heater. The oven is enclosed in a plastic (PEEK) vacuum chamber to reduce the heat dissipation and air convection. The water cooled vacuum chamber also acts as the frame for triaxial magnetic coils. The vacuum chamber is enclosed in five layers of μ -metal magnetic shielding, and an inner Mn-Zn ferrite shield used to minimize the Johnson-current magnetic noise. The probe light is polarization modulated with a photoelectric modulator (PEM) and demodulated with a lock-in amplifier to avoid the low-frequency noise. The pump and probe lasers are frequency- and amplitude-stabilized, as described in Supplementary Information of Ref. [24]. PBS stands for polarization beam splitter.

optically-thin K atoms, with a light intensity of approximately 450 mW/cm^2 . The optically-thick Rb atoms undergo spin polarization through spin-exchange collisions with K atoms, thereby reducing strong light absorption by the optically-thick alkali atoms and improving the spin polarization homogeneity of alkali atoms. Furthermore, the ^{21}Ne nuclear spins are polarized through spin-exchange collisions with alkali atoms, primarily Rb atoms.

A linearly polarized probe light along the x axis measures the transverse component of electronic spin polarization of Rb atoms based on the optical rotation. The frequency of probe light is tuned to the low-frequency side of D1-line of Rb by about 240 GHz. Glan-Taylor prisms with an extinction ratio of about 100000:1 are used as polarizer and analyzer in the probe light path. The probe light, modulated by a photoelastic modulator at 50 kHz, isolates low-frequency noise. Pump and probe lasers, closed-loop stabilized with liquid crystal variable retarders (LCVR), consist of a laser diode from Eagleyard and a homemade control system. Additional key details of the experimental setup include the electronic spin polarization of approximately 0.5, the electronic spin relaxation rate of about 3380 rad/s, the nuclear spin polarization of approximately 0.07 and the nuclear spin

relaxation rate of about 0.06 rad/s measured in the SC regime.

Dynamics of Hybrid Spin Resonance

The collective polarizations of alkali and noble-gas spins are described by $\mathbf{P}^e = \langle \mathbf{S}_e \rangle / S_e$ and $\mathbf{P}^n = \langle \mathbf{K}_n \rangle / K_n$, respectively. In this context, \mathbf{S}_e represents the valence electron spin operator (with $S_e = 1/2$) of the alkali atom, while \mathbf{K}_n denotes the nuclear spin of the noble-gas atoms ($K = 1/2$ for ^3He and $K = 3/2$ for ^{21}Ne). The dynamics of these spins, which occupy the same volume (i.e., the glass cell), can be characterized by the Bloch equations, which couple the alkali electron spin polarization \mathbf{P}^e with the noble-gas nuclear spin polarization \mathbf{P}^n [29].

$$\begin{aligned} \frac{\partial \mathbf{P}^e}{\partial t} &= \frac{\gamma_e}{Q} \left(\mathbf{B} + \mathbf{B}^n + \mathbf{b}^e - \Omega \frac{Q}{\gamma_e} + \mathbf{L}^e \right) \times \mathbf{P}^e \\ &\quad + \frac{R_p S_z^p + R_{se}^{\text{ne}} \mathbf{P}^n}{Q} - \frac{\{R_1^e, R_2^e, R_2^e\}}{Q} \mathbf{P}^e + D_e \nabla^2 \mathbf{P}^e, \\ \frac{\partial \mathbf{P}^n}{\partial t} &= \gamma_n \left(\mathbf{B} + \mathbf{B}^e + \mathbf{b}^n - \frac{\Omega}{\gamma_n} \right) \times \mathbf{P}^n \\ &\quad + R_{se}^{\text{en}} \mathbf{P}^e - \{R_1^n, R_2^n, R_2^n\} \mathbf{P}^n + D_n \nabla^2 \mathbf{P}^n. \end{aligned} \quad (\text{A.1})$$

The first equation describes the dynamics of alkali electron spins, while the second equation describes the dynamics of noble-gas nuclear spins. Each equation consists of four terms on the right-hand side. The first term describes the spin precession of the spin ensemble. Alkali electron spins precess under the sum of a classical magnetic field \mathbf{B} , an effective field \mathbf{B}^n from the noble-gas spins, an exotic field coupling to the electron spins due to ultralight dark matter \mathbf{b}^e , an inertial rotation Ω , and an AC Stark light shift \mathbf{L}^e . Similarly, noble-gas spins precess under the sum of \mathbf{B} , an effective field \mathbf{B}^e from the alkali spins, an exotic field coupling to the nuclear spins due to ultralight dark matter \mathbf{b}^n , and Ω . Here, γ_e and γ_n represent the gyromagnetic ratios of alkali electrons and noble-gas nuclei, respectively. Q is the slowing-down factor of alkali atoms considering the hyperfine interaction from its nuclear spin.

The second term of each equation describes the spin polarization of alkali and noble-gas spins. Alkali spins are optically polarized using circularly polarized pump light at a pumping rate R_p , with photon spin $S_z^p \approx 1$. Additionally, alkali spins are polarized via spin-exchange collisions with noble-gas spins at a rate R_{se}^{ne} , which is negligible compared to the pumping rate R_p . Conversely, noble-gas spins are polarized via spin-exchange collisions with alkali spins at a rate R_{se}^{en} .

The third term of each equation describes the spin relaxation of the spin ensemble. The longitudinal and transverse spin components of alkali spins relax at rates R_1^e and R_2^e , respectively, while the longitudinal and transverse spin components of noble-gas spins relax at rates R_1^n and R_2^n , respectively. The final term of each equation characterizes the diffusion of each spin species, where D_e and D_n represent the diffusion constants of alkali and noble-gas atoms, respectively.

When a small transverse excitation is introduced, the longitudinal components of spin polarizations, P_z^e and P_z^n , remain nearly unchanged and are equal to their respective equilibrium values, $P_{z0}^e = R_p S_z^p / R_1^e$ and $P_{z0}^n = P_{z0}^e R_{se}^n / R_1^n$. Therefore, the longitudinal components can be factored out of the coupled Bloch equations. To reduce the number of equations, the transverse components of alkali and noble-gas spins can be expressed as $P_\perp^e = P_x^e + iP_y^e$ and $P_\perp^n = P_x^n + iP_y^n$, respectively.

The dynamic response of the coupled alkali and noble-gas spin ensembles can be determined by solving the coupled Bloch equations. In this experiment, we measure the transverse component of alkali spins, $P_x^e(t)$, which can be expressed as:

$$P_x^e(t) = \text{Re}[P_1 e^{-(\Gamma_e + i\Omega_e)t} + P_2 e^{-(\Gamma_n + i\Omega_n)t}] + P_0, \quad (\text{A.2})$$

where the two exponential terms correspond to the alkali and noble-gas spins, respectively. The parameters Γ_e and Ω_e represent the decay rate and precession frequency of the alkali spins, while Γ_n and Ω_n correspond to the noble-gas spins. The coefficients P_1 , P_2 , and P_0 are dependent on the specific working conditions. The decay rate and precession frequency of each spin species are interconnected with those of the other species, and can be expressed as:

$$\begin{aligned} \Gamma_e &= \frac{R_2^e/Q + R_2^n}{2} + \frac{1}{2\sqrt{2}} \sqrt{\sqrt{a^2 + b^2} + a}, \\ \Omega_e &= -\frac{\omega_z^e + \omega_z^n}{2} + \frac{1}{2\sqrt{2}} \text{Sign}(b) \sqrt{\sqrt{a^2 + b^2} - a}, \\ \Gamma_n &= \frac{R_2^e/Q + R_2^n}{2} - \frac{1}{2\sqrt{2}} \sqrt{\sqrt{a^2 + b^2} + a}, \\ \Omega_n &= -\frac{\omega_z^e + \omega_z^n}{2} - \frac{1}{2\sqrt{2}} \text{Sign}(b) \sqrt{\sqrt{a^2 + b^2} - a}, \end{aligned} \quad (\text{A.3})$$

where the parameters a and b are given by

$$\begin{aligned} a &= (R_2^e/Q - R_2^n)^2 - (\omega_z^e - \omega_z^n)^2 + 4R_{se}^{ne} R_{se}^{en}/Q - 4\omega_z^{ne} \omega_z^{en}, \\ b &= -2(R_2^e/Q - R_2^n)(\omega_z^e - \omega_z^n) - 4(R_{se}^{ne} \omega_z^{en}/Q + R_{se}^{en} \omega_z^{ne}), \end{aligned} \quad (\text{A.4})$$

where $\omega_z^e = \gamma_e(B_z^n + B_z)/Q$, $\omega_z^n = \gamma_n(B_z^e + B_z)$, $\omega_z^{ne} = \gamma_e \lambda M_0^n P_z^e / Q$, and $\omega_z^{en} = \gamma_n \lambda M_0^e P_z^n$.

The coupling between alkali spins and noble-gas spins is determined by the dominant field B_z . When B_z is much greater than B_z^n , the dynamics of alkali spins and noble-gas spins are decoupled. The alkali spins decay and precess based on their own relaxation rate R_2^e/Q and precession frequency $\gamma_e(B_z + B_z^n)/Q$, while noble-gas spins exhibit similar behavior, with a relaxation rate R_2^n and a precession frequency of $\gamma_n(B_z + B_z^e)$. However, at the HSR point, alkali and noble-gas spins become resonantly-coupled. This leads to hybridization between noble-gas spins and alkali spins, resulting in the maximum decay and precession rates for noble-gas spins.

The responses to oscillation input signals along transverse direction can be obtained by solving the coupled Bloch

equations. The response to oscillating magnetic field $B_y = B_{y0} \cos(\omega t)$ is

$$\begin{aligned} P_{x(B_y)}^e &= K_{B_y} B_{y0} \cos(\omega t + \phi_{B_y}), \\ K_{B_y} &\approx \frac{\gamma_e P_z^e}{Q} \frac{\omega}{\left\{ (\omega_z^n \omega_z^e - \omega^2)^2 + (R_2^e/Q \times \omega)^2 \right\}^{1/2}}, \end{aligned} \quad (\text{A.5})$$

where K_{B_y} is the scale factor, $\omega_z^n = \gamma_n B_z^n$, and $\omega_z^e = \gamma_e B_z^e / Q$.

The response to oscillation exotic field coupled to noble-gas spins $b_x^n = b_{x0}^n \cos(\omega t)$ is

$$\begin{aligned} P_{x(b_x^n)}^e &= K_{b_x^n} b_{x0}^n \cos(\omega t + \phi_{b_x^n}), \\ K_{b_x^n} &\approx \frac{\gamma_e P_z^e}{Q} \frac{\omega_z^n}{\left\{ (\omega_z^n \omega_z^e - \omega^2)^2 + (R_2^e/Q \times \omega)^2 \right\}^{1/2}}. \end{aligned} \quad (\text{A.6})$$

The scale factors for magnetic field B_y and exotic field b_x^n have the following relation $K_{B_y} = K_{b_x^n} \omega / \omega_z^n$. As a result, the response to oscillating magnetic fields can be used to calibrate the response to exotic fields, which is a conventional calibration method in atomic magnetometer.

Axion Signal Analysis

DM Signal Calculations

The signal measured in a time sequence can be expressed as the projection of this pseudomagnetic field in the direction of the sensitive axis $\hat{\mathbf{m}}$ at discrete points in time:

$$\beta_j = \frac{g_{aNN}}{\gamma_n} \nabla a(j\Delta t) \cdot \hat{\mathbf{m}}(j\Delta t), \quad (\text{A.7})$$

where $\Delta t = 1/(3598 \text{ Hz})$ is the sampling interval time, and j is an integer index, with $j = N$ corresponding to the total measurement time. As a result of the Earth rotation, the sensitive axis $\hat{\mathbf{m}}(t)$ changes with time. The daily modulation effect caused by the Earth rotation can be expressed as

$$\hat{\mathbf{m}}_i(j\Delta t) \approx \mathbf{C}_i \cos(\omega_E j\Delta t + \theta_i) + \mathbf{D}_i, \quad (\text{A.8})$$

where ω_E is the angular frequency of the Earth rotation, and the parameters \mathbf{C}_i , \mathbf{D}_i , and θ_i are determined by the location, the sensitive axis, and the starting time of the experiment respectively. The index i runs from an orthonormal coordinate system $\{\hat{u}, \hat{v}, \hat{s}\}$ [18], where \hat{v} is parallel to the Earth velocity respect to the Sun. The parameters for Dataset 1 and 2 are given in Table I.

We calibrated the system every four hours to monitor the status during data acquisition. The system was verified to be stable in Ref. [24]. For higher-frequency signal, we carried out a 209-hr measurement with an 86% duty cycle (Dataset 1), resulting in a measured power spectral density (PSD) data step of $\Delta f = 1/(180 \text{ hr}) = 1.54 \mu\text{Hz}$. Additionally, we performed a 4-hr continuous measurement with a nearly identical setup deployed in an underground laboratory (Dataset 2), which provided better suppression of vibrations and power-line interference. Both measurements were conducted at a fixed bias

	C_i	D_i	θ_i (DS-1)	θ_i (DS-2)	θ_i (DS-3)
\hat{u}	0.89	0	0.37	2.0	-2.9
\hat{v}	0.67	0	-0.59	1.0	2.5
\hat{s}	0.88	0	-1.5	0.12	1.6

TABLE I. The parameters for the experiment setup. C_i and D_i are the same for Dataset (DS) 1, 2 and 3, because they are taken at nearly the same location. $D_i = 0$ because the sensitive axis points to the West. The phases θ_i (DS-1, DS-2, DS-3) are determined by the starting time of each data set.

magnetic field in the HSR regime. Subsequently, we transformed the two data sets into the frequency domain using non-uniform Fast Fourier Transformation (FFT). Since the data have gaps, one has to use the non-uniform FFT. To accommodate memory constraints (128 GB of random access memory in the computer we used), we had to down-sample the data by a factor of two, which limited the highest frequency it could accommodate to 900 Hz. Since there is no down-sampling in Dataset 2, it can cover the frequency range up to $f_s/2$; we studied the frequencies up to 1000 Hz and Dataset 2 was the only one with which we could access the [900, 1000] Hz range. We employed the log-likelihood ratio (LLR) test to analyze the two data sets separately in the frequency domain for the axion-neutron g_{ann} coupling scenario, accounting for the stochastic effect [18]. The effective coupling between axion and the nucleus N is given by $g_{aNN} = \xi_n^{\text{Ne}} g_{ann} + \xi_p^{\text{Ne}} g_{app}$, where $\xi_n^{\text{Ne}} = 0.58/3$ and $\xi_p^{\text{Ne}} = 0.04/3$ are the fractions of spin-polarization for neutron and proton in ^{21}Ne [53, 54]. The factor of 3 is a rescaling factor due to the ^{21}Ne spin $3/2$.

To measure low-frequency signals, where magnetic noise is particularly significant, we use the SC regime [29]. In this regime, the noble-gas magnetization automatically compensates low-frequency magnetic fields, leaving alkali spins protected from magnetic noise. The $\text{K-}^3\text{He}$ SC comagnetometers have shown ultrahigh sensitivity of about $1 \text{ fT/Hz}^{1/2}$ [55]. In our experiment, we use ^{21}Ne whose gyromagnetic ratio, $\gamma_{\text{Ne}} = (2\pi) \times 3.36 \text{ MHz/T}$, is one order of magnitude smaller than that of ^3He . This results in higher sensitivity to exotic field under the same noise level [25]. The SC comagnetometer can be calibrated by oscillation magnetic field [56] using the residual response of the SC magnetometer proportional to the frequency of the oscillation at low frequencies. The frequency response to exotic fields coupling to noble-gas nuclear spins is then calibrated by that of magnetic field, in the same way as it is done in the HSR regime.

The SC regime data were taken over 146 hr, which is considerably shorter than the 40-day duration of the $\text{K-}^3\text{He}$ data taking in Ref. [18]. To make the most of the available data, we calculate the power spectral density (PSD) for each hour separately. We then removed the lowest-quality 10% of the data (specifically, one-hour long data segments showing the largest fluctuations), resulting in a final dataset of 132 hr for the analysis. We note that this procedure suppresses transient stochastic signals that are being searched for in experiments like GNOME [48]. The analysis

of SC data is similar to that for the HSR data and we have derived DM constraints in the frequency range of [0.01, 6] Hz.

Data Preparation

The information regarding the start date, end date, and measurement duration for the three datasets is presented in Table II. In Dataset 2 for HSR, we utilized a distinct apparatus situated in an 8-meter-deep underground basement. This facility was originally designed as an air-defense structure and includes a substantial cistern, which contributes to temperature stability and reduced vibration noise compared to Dataset 1. Unfortunately, we were unable to extend the measurement duration of Dataset 2 due to ongoing construction and renovation activities. However, once these construction efforts are completed, we intend to relocate our future experiments to this deep underground site.

Dataset	Start Date	End Date	Duration [hr]
HSR (Dataset 1)	2023/01/16	2023/01/25	209
HSR (Dataset 2)	2023/01/18	2023/01/18	4
SC (Dataset 3)	2023/03/31	2023/04/09	146

TABLE II. Information regarding the three datasets. All data were collected in the laboratory located in Hangzhou, China.

In our analysis of the axion dark matter signal, we define the analysis frequency band as detailed in Table III. To effectively determine an upper limit for the axion-nucleon coupling strength through the profile log-likelihood analysis, it is crucial that the analysis band spans the complete axion signal linewidth. Furthermore, it is noteworthy that the Earth rotation introduces a $\pm f_E$ modulation to the signal frequency, with $f_E \approx 11.6 \mu\text{Hz}$ representing its rotational frequency.

For the low-frequency range, mostly corresponding to the SC regime (Dataset 3), $f_a \in [0.01, 6] \text{ Hz}$, the Earth rotation effect becomes significant due to the fact that f_E can easily surpass the signal line width, approximately on the order of $\Delta f_a \approx 10^{-6} f_a$. Therefore, the selection of our noise frequency band is critical and should encompass the frequency shift induced by the Earth rotation. Moreover, to obtain a more precise assessment of the background noise level, we include approximately 200-300 data bins in the log-likelihood analysis. As a result, we have chosen the range $[f_a - 20\Delta f_E, f_a + 20\Delta f_E]$ as our analysis frequency band for Dataset 3. This range remains adequately narrow to uphold the assumption of white noise in the background.

Axion Frequency (f_a [Hz])	Frequency band used for analysis
[0.01, 6]	$[f_a - 20\Delta f_E, f_a + 20\Delta f_E]$
[6, 1000]	$[f_a - \frac{3}{2}\Delta f_a, f_a + 3\Delta f_a]$

TABLE III. The frequency bands utilized for the log-likelihood profile analysis, with $f_E \approx 11.6 \mu\text{Hz}$ being Earth rotational frequency, and Δf_a representing the signal linewidth.

In the context of the high-frequency range, mostly associated with the HSR regime (Dataset 1 and 2), where f_a falls

within the interval $[6, 1000)$ Hz, the impact of Earth rotation becomes smaller and $\Delta f_a \geq f_E$. For instance, when f_a is approximately 6 Hz, the signal linewidth is estimated to be around $\Delta f_a \approx 10.1 \mu\text{Hz}$, which is roughly the frequency of Earth rotation. For the increased axion frequency, the impact of Earth rotation becomes negligible. Therefore, the choice of bandwidth fully includes the modulation of axion signal linewidth. This band choice is intentionally asymmetric, because the total energy of the axion includes its rest mass energy and the kinetic energy.

In this study, we employed the MATLAB built-in non-uniform FFT algorithm, derived from Refs. [57, 58], which is based on the z -transform method. The z -transform is a generalization of the Fourier transform for discrete series, making it suitable for handling non-uniform time series data. In Ref. [59], the study showed the consistency of the z -transform FFT algorithm with the Lomb-Scargle algorithm, which was used in the $\text{K-}^3\text{He}$ study [18]. We also generated non-uniform random test data to compare both algorithms and found negligible differences in the frequency power spectrum density. As a result, we chose to adopt the MATLAB built-in z -transform FFT algorithm for its accuracy and convenience.

Likelihood Analysis

We now briefly introduce the method for setting the limits below, which is based on Ref. [18]. The time sequence of $\beta_1, \beta_2, \dots, \beta_N$ follows a multivariate normal distribution with zero means due to the uniform random phase ϕ_p contained in each \mathbf{p} mode of the axion, in accordance with the central limit theorem. As a result, the upper limits on axion coupling g_N must utilize the statistical properties.

The Fourier transform of the time series β_j produces a complex variable $\tilde{\beta}_k$, which follows a multivariate normal distribution. The frequency series can be redefined in terms of its real and imaginary parts,

$$A_k \equiv \frac{2}{N} \text{Re}[\tilde{\beta}_k], \quad B_k \equiv -\frac{2}{N} \text{Im}[\tilde{\beta}_k]. \quad (\text{A.9})$$

Since A_k and B_k have zero means, their statistical properties are coded in the covariance matrix $\text{Cov}[A_{k_1}, A_{k_2}]$, $\text{Cov}[B_{k_1}, A_{k_2}]$, $\text{Cov}[A_{k_1}, B_{k_2}]$ and $\text{Cov}[B_{k_1}, B_{k_2}]$ with $(A/B)_{k_1/k_2}$ being the specific choices of $(A/B)_k$. Their calculations are detailed in Ref. [18]. Furthermore, if the duration of data taking T is much greater than the coherence time τ_a , the covariance matrix calculation can be significantly simplified.

The experimental background within a sufficiently narrow bandwidth can be modeled as Gaussian white noise with a zero mean and variance σ_b^2 . Let the measured data in the frequency domain be the vector $\mathbf{d} = \{A_k, B_k\}$, with a variance matrix given by $\Sigma = \Sigma_a + \sigma_b^2 \mathbb{1}$. Here, $\Sigma_a(g_{aNN}, m_a)$ is the covariance matrix of the axion signal, which depends on the coupling g_{aNN} and the axion mass m_a , while $\mathbb{1}$ is the identity matrix corresponding to the Gaussian white noise [18]. The

covariance matrix of the axion signal is explicitly given by

$$\Sigma_a(g_{aNN}, m_a)_{k,r} = \begin{pmatrix} \text{Cov}(A_k, A_r) & \text{Cov}(A_k, B_r) \\ \text{Cov}(B_k, A_r) & \text{Cov}(B_k, B_r) \end{pmatrix}, \quad (\text{A.10})$$

where the dependence on the frequency bin indices k and r ensures that the full shape of the axion signal is encoded within it. Consequently, the axion signal, including its stochastic effects, is fully captured by Σ_a . Since both the signal and the background are multivariate Gaussian random variables, one can finally construct the likelihood function as [18, 37],

$$L(\mathbf{d}|g_{aNN}, \sigma_b^2) = \frac{1}{\sqrt{(2\pi)^{2N} \det(\Sigma)}} \exp\left(-\frac{1}{2} \mathbf{d}^T \Sigma^{-1} \mathbf{d}\right). \quad (\text{A.11})$$

Calculation of Axion Limits

To set a quantitative limit, one can use the log-likelihood ratio (LLR) below [18]

$$\text{LLR}(g_{aNN}) = \begin{cases} -2 \log \left[\frac{L(g_{aNN}, \tilde{\sigma}_b)}{L(\hat{g}, \tilde{\sigma}_b)} \right], & \hat{g} \leq g_{aNN} \\ 0, & \hat{g} > g_{aNN} \end{cases} \quad (\text{A.12})$$

where $\tilde{\sigma}_b$ maximizes L for a fixed nucleus coupling g_{aNN} . In order to establish an upper limit, $\text{LLR} = 0$ if $\hat{g} > g_{aNN}$. The 95% CL upper limits are set by finding the value of g_{aNN} where $\text{LLR}(g_{aNN}) = 2.71$. Finally, we calculate the two sets of data separately and choose the stronger limits on g_{aNN} among the two. By applying the spin polarization fractions in ^{21}Ne , the limits on the nucleus coupling g_{aNN} can be converted to nucleon couplings g_{ann} and g_{app} , resulting in the final outcome displayed in Fig. 4 of the main text. To set a continuous limit at axion mass parameter spaces, the limit frequencies are separated by $\Delta f = 1/(2\tau_a)$, leading to over 10 millions of limits points.

For $f_a \in [3, 30]$ Hz, the sensitivity to g_{ann} remains approximately constant at a level of about $3 \times 10^{-9} \text{GeV}^{-1}$, while for $f_a \in [30, 1000]$ Hz, it is roughly proportional to f_a^2 . The shape of the curve is determined by the sensitivity to the magnetic field B_y and the ratio between the two responses $K_{B_y}/K_{b_y} \propto \omega_a$. Neglecting the stochastic effect, the sensitivity to the axion signal at frequency f_a can be estimated from the square root of the data power spectrum, denoted as σ_b which is the standard deviation of B_y . The 95% confidence level (CL) limit can be obtained by roughly letting $g_{ann} \approx (2.7\sigma_B K_{B_y}/K_{b_y})/(\xi_n \sqrt{\rho_{\text{DM}} v_{\text{DM}}}/\gamma_n)$. Therefore, the coupling g_{ann} is proportional to $f_a \sigma_b$. In the PSD data, we observed that σ_B is proportional to f_a^{-1} for $f_a \in [3, 30]$ Hz, flat for $f_a \in [30, 50]$ Hz, and proportional to f_a for $f_a \in [50, 1000]$ Hz. Including the stochastic effect will enlarge the coupling g_{ann} by a factor of a few, but it has no significant dependence on f_a . Therefore, the slope of g_{ann} in the final results matches the simple estimation above quite well.

In alkali-noble gas hybrid sensors, the energy resolution for measuring the shifts of the levels of the noble-gas nuclear spins is typically much higher than that for alkali spins, primarily because the higher atom density, longer coherence

time and smaller magnetic moment [60]. Old K-³He comagnetometer data can set limits on the axion neutron coupling in the frequency below 10 Hz. There are two results interpreted by the same experiment. In Fig. 4 of the main text, we only plot the limits using the original data and properly treated the stochastic effects of axion [18], and ignore the one that indirectly interpreted the results from published power spectra [61]. Our SC data provides comparable and even stronger limits to the K-³He study [18] for the axion-neutron coupling g_{ann} . In terms of the axion-proton coupling g_{app} , we have achieved the most stringent terrestrial constraints across an extensive frequency range of $[10^{-2}, 7 \times 10^2]$ Hz. The K-³He results can also provide limits on the axion-proton coupling. However, considering the spin polarization fractions in ³He, with $\xi_n^{^3\text{He}} = 87\%$ and $\xi_p^{^3\text{He}} = -2.7\%$ [55], we found that their constraints are approximately two times weaker than ours.

In addition to the linear axion derivative coupling, we investigated the limits on the quadratic coupling scenario [16, 20, 62, 63] following a similar procedure as for linear coupling. The corresponding Hamiltonian can be expressed as:

$$\mathcal{H}_{\text{quad}} = g_{\text{quad}}^2 \nabla a^2 \cdot \mathbf{I}. \quad (\text{A.13})$$

Assuming that the quadratic coupling dominates, we can use the same analysis as above to recast it as results on g_{quad} . These are presented in Fig. 6. As a result of the quadratic coupling, the range of axion frequencies is reduced by a factor of two compared to the linear coupling, resulting in a range of $[5 \times 10^{-3}, 5 \times 10^2]$ Hz. The limits surpass the astrophysical constraints by several orders of magnitude for $f_a \lesssim 150$ Hz. These results also surpass the earlier terrestrial experiments.

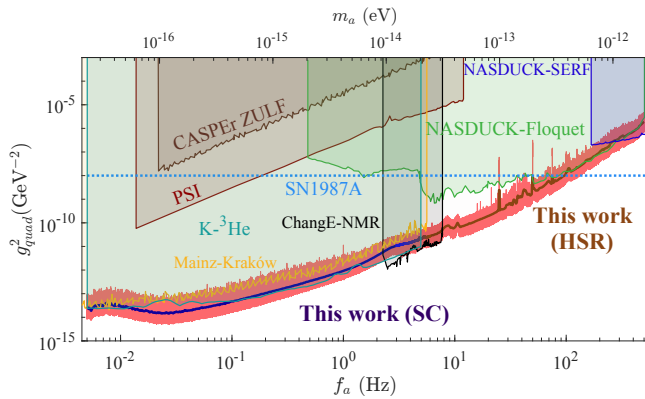


FIG. 6. The 95% C.L. upper limits (depicted by red lines) for the quadratic neutron coupling g_{quad}^2 are derived from measurements in both the SC and HSR regimes, using the same labels as in Fig. 4 of the main text.

Post-Analysis of the Possible Candidates.

We explore if there are possible axion DM signal in the data. For a quantitative analysis of possible axion candidates, we define the following test statistics to test the significance of

a best-fit signal compared to the background only model [18],

$$\text{LLR}_{\text{discover}} = \begin{cases} -2 \ln \left[\frac{L(0, \hat{\sigma}_b)}{L(\hat{g}, \hat{\sigma}_b)} \right], & \hat{g} \geq 0 \\ 0, & \hat{g} < 0, \end{cases} \quad (\text{A.14})$$

where $\hat{\sigma}_b$ maximizes LLR without the signal, while \hat{g} and $\hat{\sigma}_b$ maximize LLR for a two variable marginalization.

Taking into account the look-elsewhere effect, we conservatively estimate that $\text{LLR} > 52.1$ corresponds to a one-sided global significance of 5σ . We found that out of the 6.8 million tested masses, 36600 candidates exceeded the 5σ confidence level, which accounts for approximately 0.5% of Dataset 1. It is evident that there is systematic noise present in Dataset 1, which is not adequately accounted for by the assumption of random Gaussian noise. Regarding the potential sources of systematic noise in Dataset 1, significant power grid noise in the harmonics of 50 Hz was observed when examining the power spectrum density of the data. Furthermore, due to the extended measurement time, the drift of the power line noise contributes to broadening the noise range. Additionally, at low frequencies, vibration peaks were detected around 6 Hz and from 17 to 23 Hz, as confirmed using a commercial seismometer.

Fortunately, Dataset 2 possesses superior noise control within the clean underground environment. Initially, we cross-check the candidate frequencies for their 5σ significance level in Dataset 2, incorporating the look-elsewhere effect. No candidates are identified beyond the 5σ level, indicating the absence of significant systematic noise in Dataset 2. In determining the final sensitivity result, the combined sensitivity is derived by selecting the superior sensitivity between Dataset 1 and Dataset 2.

Among the 36600 candidates, 62 exhibit better sensitivity in Dataset 1 than in Dataset 2 ($g_{\text{aNN}}^{\text{D1}} < g_{\text{aNN}}^{\text{D2}}$). Consequently, the remaining candidates are replaced by the improved limits from Dataset 2, aligning with the random Gaussian noise assumption and ensuring the robustness of their 95% exclusion limits. This process leads to a significant reduction in the number of high LLR points, now totaling only 62, constituting a small fraction of approximately 10^{-5} .

Subsequently, the remaining 62 candidates undergo further scrutiny using Dataset 1. Three distinct tests are employed to explore their potential as dark matter candidates: the two-stage joint-LLR test, the signal-strength-stability test, and the signal-shape analysis.

(1) **The Two-Stage Joint-LLR test:** In this test, the objective is to ascertain whether the identified candidates can be attributed to transient systematic noise. Therefore, we divided Dataset 1 into two parts, each with an equal duration of 90 hours. For two datasets, 1A and 1B, of the same size, these two datasets can be considered independent, given that the time span of 90 hours significantly exceeds the coherence time of the smallest axion frequency among the 62 candidates. Thus, the joint-likelihood function can be constructed as fol-

Frequency [Hz]	Full-data LLR	Joint-LLR	Sig-Stability	Sig-Shape	Frequency [Hz]	Full-data LLR	Joint-LLR	Sig-Stability	Sig-Shape
46.704996	69.77	✓ (68.)	✓	✗	81.504437	56.57	✗ (5.87)		
48.391586	53.88	✗ (2.49)			81.722087	109.95	✗ (14.8)		
67.129321	69.04	✗ (0.06)			81.754539	53.81	✗ (1.24)		
67.143839	75.89	✓ (31.36)	✗		81.841119	60.90	✗ (11.3)		
67.162956	54.79	✗ (18.79)			97.660449	79.31	✓ (84.27)	✓	✗
67.164261	65.76	✗ (2.67)			134.141313	57.61	✗ (6.94)		
67.239592	80.46	✗ (0)			134.248211	66.08	✗ (9.1)		
67.256066	68.44	✗ (9.16)			134.451359	76.66	✗ (7.91)		
67.299372	59.97	✗ (0)			134.454312	64.66	✗ (2.27)		
67.305285	52.94	✗ (0.03)			134.459877	54.65	✗ (9.20)		
67.372806	75.25	✗ (0.95)			137.940287	71.64	✗ (0.13)		
67.378668	96.18	✗ (7.01)			138.303853	54.19	✗ (4.01)		
67.384759	58.44	✗ (0)			140.709636	70.36	✗ (8.71)		
67.399959	55.77	✗ (0.68)			140.717362	59.57	✗ (1.47)		
67.401895	62.05	✗ (0.07)			140.733529	58.62	✓ (31.01)	✗	
67.424104	55.74	✗ (0.11)			140.736620	53.61	✗ (21.57)		
67.439142	68.60	✗ (1.72)			140.791675	72.28	✗ (3.85)		
67.447232	70.18	✗ (9.51)			140.794648	52.74	✗ (17.40)		
67.457887	90.58	✗ (6.36)			141.246730	62.39	✗ (16.18)		
72.782530	60.67	✗ (12.03)			141.701699	96.47	✓ (23.71)	✗	
72.785297	52.33	✗ (16.78)			141.952935	63.83	✗ (0.05)		
72.788802	56.44	✗ (1.17)			142.624594	79.79	✗ (6.57)		
72.797656	53.53	✗ (3.07)			142.729812	65.91	✓ (27.34)	✗	
72.803745	61.79	✗ (0.3)			143.372442	62.12	✗ (9.34)		
72.823120	58.99	✗ (0)			143.969920	55.22	✗ (2.41)		
72.825273	52.13	✗ (10.92)			157.812307	63.13	✗ (4.07)		
72.839546	57.13	✗ (10.5)			159.152266	68.58	✓ (48.39)	✗	
72.869210	83.03	✗ (0.53)			161.744217	64.57	✓ (76.18)	✓	✗
72.871118	52.66	✗ (6.26)			186.715234	75.55	✓ (43.96)	✗	
72.874196	80.23	✗ (3.91)			188.360579	86.56	✓ (47.25)	✗	
72.921797	60.32	✗ (0)			363.317150	120.56	✓ (142.83)	✓	✗

TABLE IV. The flowchart illustrates the discrimination process for the 62 candidates, involving the two-stage joint-LLR test (threshold at 23.7), signal-strength-stability test, and signal-shape test. In the second column, the full-data LLR results are presented for comparison with the joint-LLR results. None of the candidates passed all three tests.

Frequency [Hz]	Dataset 1A [GeV ⁻¹]	Dataset 1B [GeV ⁻¹]	Signal Stability?
46.704996	$[2.74 \times 10^{-9}, 4.26 \times 10^{-9}]$	$[2.52 \times 10^{-9}, 4.18 \times 10^{-9}]$	✓
67.143839	$[2.17 \times 10^{-9}, 3.97 \times 10^{-9}]$	$[7.66 \times 10^{-9}, 1.10 \times 10^{-8}]$	✗
97.660449	$[6.79 \times 10^{-9}, 1.02 \times 10^{-8}]$	$[6.93 \times 10^{-9}, 1.02 \times 10^{-8}]$	✓
140.733529	$[1.37 \times 10^{-8}, 1.89 \times 10^{-8}]$	[N/A, 7.59×10^{-9}]	✗
141.701699	$[1.85 \times 10^{-8}, 2.49 \times 10^{-8}]$	$[6.25 \times 10^{-10}, 8.16 \times 10^{-9}]$	✗
142.729812	$[1.95 \times 10^{-8}, 2.83 \times 10^{-8}]$	$[5.66 \times 10^{-9}, 1.07 \times 10^{-8}]$	✗
159.152266	$[2.03 \times 10^{-8}, 2.91 \times 10^{-8}]$	$[9.46 \times 10^{-9}, 1.62 \times 10^{-8}]$	✗
161.744217	$[1.32 \times 10^{-8}, 2.02 \times 10^{-8}]$	$[1.35 \times 10^{-8}, 1.99 \times 10^{-8}]$	✓
186.715234	[N/A, 1.27×10^{-8}]	$[2.51 \times 10^{-8}, 3.29 \times 10^{-8}]$	✗
188.360579	[N/A, 1.57×10^{-8}]	$[3.1 \times 10^{-8}, 4.04 \times 10^{-8}]$	✗
363.317150	$[8.20 \times 10^{-8}, 1.13 \times 10^{-7}]$	$[9.34 \times 10^{-8}, 1.21 \times 10^{-7}]$	✓

TABLE V. The table presents the signal-strength intervals calculated at the 90% confidence level for the 11 remaining candidates after the joint-LLR two-stage test. As recommended in Ref. [18], if the signal strength intervals for Dataset 1A and 1B do not overlap, the possibility of the candidate being a dark matter signal can be excluded. The notation “N/A” means that, no solution is found for the lower threshold $g_{\text{aNN}}^{\text{lower}}$ at 90% confidence level.

lows:

$$L(g_{\text{aNN}}, \sigma_{b1A}, \sigma_{b1B}) \equiv L_{1A}(g_{\text{aNN}}, \sigma_{b1A}) \times L_{1B}(g_{\text{aNN}}, \sigma_{b1B}), \quad (\text{A.15})$$

where σ_{b1A} and σ_{b1B} represent the noise levels of the two

datasets. Following a similar approach as in the main text, the log-likelihood ratio for joint-significance is defined as:

$$\text{LLR}_{\text{discover}}^{\text{joint}} = \begin{cases} -2 \ln \left[\frac{L(0, \hat{\sigma}_{b1A}, \hat{\sigma}_{b1B})}{L(\hat{g}, \hat{\sigma}_{b1A}, \hat{\sigma}_{b1B})} \right], & \hat{g} \geq 0, \\ 0, & \hat{g} < 0, \end{cases} \quad (\text{A.16})$$

where the hats and the tildes represent the marginalization of these parameters in the denominator and numerator, respectively.

The joint-LLR, as defined, serves the purpose of distinguishing transient noise peaks from persistent signal-like peaks using the two-stage datasets. In the flowchart Table IV, we have tabulated the joint-LLR results alongside the full-data LLR for clear comparison. It is evident that many of the joint-LLR values are significantly lower when compared to the LLR, suggesting that these candidates likely originate from transient noise backgrounds.

It is worth noting that at specific test frequencies, we have obtained nearly zero joint-LLR results. These candidates exhibit a common characteristic: the noise levels of the two datasets vary significantly, and the noise peak at that particular test frequency only appears in the noisier dataset. Consequently, the joint-LLR is calculated to be very small, approaching zero, as no signal is required to fit the data under these circumstances.

In Table IV, 11 candidates out of 62 have successfully passed the joint-LLR test, with joint-LLR values exceeding the criterion of 23.7. This threshold is notably smaller than the $\text{LLR}_{\text{discover}} > 52.1$ required in the full data LLR analysis. This is because, with the identification of the frequencies of the 62 candidates, the look-elsewhere effect no longer needs to be considered in the same dataset.

(2) **The Signal-Strength-Stability Test:** In accordance with the analysis of Ref. [18], another method to distinguish noise from signal involves verifying whether the best-fit signal strength, denoted as \hat{g}_{aNN} for Dataset 1A and 1B, remains consistent throughout the entire measurement period. In this context, the best-fit signal strengths must overlap with each other. To derive the confidence interval for the best-fit \hat{g}_{aNN} , we introduce a slightly different test statistic in comparison to Eq. (A.14):

$$\text{LLR}_{\text{CL}}(g_{\text{aNN}}) = -2 \log \left[\frac{L(g_{\text{aNN}}, \tilde{\sigma}_b)}{L(\hat{g}_{\text{aNN}}, \hat{\sigma}_b)} \right]. \quad (\text{A.17})$$

It is important to note that this LLR is not set to zero for $\hat{g}_{\text{aNN}} > g_{\text{aNN}}$. This particular definition of LLR can reveal any inconsistency between the hypothesized signal strength g_{aNN} and the best-fit \hat{g}_{aNN} , regardless of whether $\hat{g}_{\text{aNN}} > g_{\text{aNN}}$ or $\hat{g}_{\text{aNN}} < g_{\text{aNN}}$. For the true signal value g_{aNN} , the cumulative distribution function (CDF) of $\text{LLR}_{\text{CL}}(g_{\text{aNN}})$ is described by the error function [64]:

$$P(\text{LLR}_{\text{CL}}(g_{\text{aNN}}) \leq y) = \text{erf} \left(\sqrt{\frac{y}{2}} \right). \quad (\text{A.18})$$

Hence, the upper and lower bounds of the confidence intervals for a confidence level CL_0 can be determined by the equations: $P[\text{LLR}_{\text{CL}}(g_{\text{aNN}}) \geq \text{LLR}_{\text{CL}}(g_{\text{aNN}}^{\text{upper/lower}})] = (1 - \text{CL}_0)/2$ for $g_{\text{aNN}}^{\text{lower}} < \hat{g}_{\text{aNN}}$ and $g_{\text{aNN}}^{\text{upper}} > \hat{g}_{\text{aNN}}$, respectively. The results for 90% confidence level intervals for the 11 test frequencies are presented in Table V. Test frequencies with

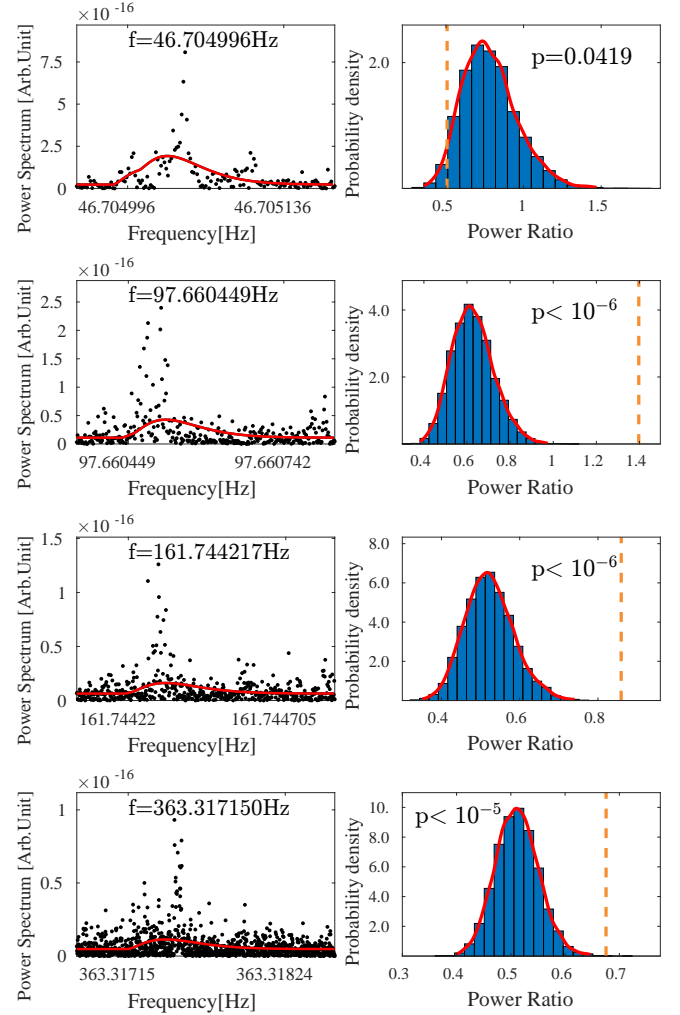


FIG. 7. *Left panel:* The black dots represent the power spectra of the data. The expected power spectra of the axion signals are shown as red solid lines. *Right panel:* The distribution of the power ratio for the axion candidate is determined through Monte-Carlo simulations and is represented as a histogram. The orange lines in the figure indicate the power ratio observed in the data, and the p -value quantifies the likelihood of obtaining this power ratio based on the distribution. The four candidates thus fail the 95% confidence-level test (the one around 46.7 Hz—only marginally) and are attributed to monochromatic noise which does not have the expected signal shape. As a result, these candidates are rejected as potential axion candidates at the 95% confidence level.

non-overlapping confidence level intervals can be excluded as potential axion signals at a 90% confidence level. Our analysis shows that there are four frequencies, namely $f_a = 46.704996, 97.660449, 161.744217, 363.317150$ Hz, that have passed the signal-strength-stability test.

(3) **The Signal-Shape Analysis:** In the final step, we need to employ signal shape information to distinguish between a persistent systematic noise peak and an axion dark matter signal. This discrimination can be achieved by either incorporat-

ing a monochromatic noise peak into the background model to assess the statistical possibility, as demonstrated in Ref. [39], because in the analysis the background was assumed to be Gaussian white noise. Alternatively, one can analyze the shape of the power spectrum density of the data and compare it with the axion signal lineshape using Monte-Carlo methods, as shown in Ref. [18].

Following the latter approach presented in Ref. [18], a power ratio PR can be defined as $PR \equiv P_1/P_2$, where P_1 represents the power in the frequency band $[f_a, f_a + \Delta f_a/2]$. In contrast, P_2 is the power in the subsequent frequency band $[f_a + \Delta f_a/2, f_a + 2\Delta f_a]$, which characterizes the power in the high-energy tail. This power ratio PR reflects the lineshape of the axion dark matter signal.

In the left panel of Fig. 7, the black dots represent the power spectra of the data while the expected power spectra of the axion signals are shown as red solid lines. We have conducted 10000 Monte-Carlo simulations for each of the four candidate frequencies, considering them as axion-dark-matter candidates. In the right panel of Fig. 7, we present the simulated distribution of the power ratio PR , depicted as blue histograms. Using the real data from the left panel, one can calculate the true power ratio of the data, shown as the orange vertical line. The p -value quantifies the likelihood of obtaining this power ratio based on the distribution. If the p -value is smaller than 0.05, we conclude that the four test frequencies are unlikely to be axion candidates at a 95% confidence level.

Three of the candidates exhibited extremely small p -values, less than 10^{-5} , indicating they are inconsistent with the axion dark matter signal shape and are most likely to be persistent systematic noise peaks. The candidate at a frequency of $f_a = 46.704996$ Hz had a p -value of 0.0419, still excluded at the 95% confidence level though marginally.

In summary, after the two-stage joint-LLR test, the signal-strength-stability test, and the signal-shape analysis, there are no candidates left as potential axion dark matter candidates. However, it is worth noting that the candidate at a frequency of $f_a = 46.704996$ Hz is marginally excluded, and further tests are encouraged.

ACKNOWLEDGEMENT

We would like to thank Junyi Lee, Yevgeny Kats and Itay Bloch for helpful discussions. The work of KW, WQ and JCF is supported by National Science Foundation of China (NSFC) under Grants No. 62203030 and 61925301 for Distinguished Young Scholars, also supported by NSFC-CAS under Grant No. XK2023XXC002, and by the Innovation Program for Quantum Science and Technology under Grant 2021ZD0300401. The work of JL is supported by NSFC under Grant No. 12475103, No. 12235001, No. 12075005, and by Peking University under startup Grant No. 7101502458. The work of XPW is supported by the NSFC under Grant No. 12375095 and the Fundamental Research Funds for the Central Universities. The work of WJ and DB is supported by

the DFG Project ID 390831469: EXC 2118 (PRISMA+ Cluster of Excellence), by the German Federal Ministry of Education and Research (BMBF) within the Quantumtechnologien program (Grant No. 13N15064), by the COST Action within the project COSMIC WISPerS (Grant No. CA21106), and by the QuantERA project LEMAQUME (DFG Project No. 500314265).

* These authors contributed equally to this work

† Corresponding author: wei.ji@pku.edu.cn

‡ Corresponding author: jiali@pku.edu.cn

§ Corresponding author: fangjiancheng@buaa.edu.cn

- [1] R. Essig and et al., “Working group report: New light weakly coupled particles,” Fermi National Accelerator Lab. (FNAL), Batavia, IL (United States); SLAC National Accelerator Lab., Menlo Park, CA (United States); Brookhaven National Lab. (BNL), Upton, NY (United States); Lawrence Livermore National Lab. (LLNL), Livermore, CA (United States); Los Alamos National Lab. (LANL), Los Alamos, NM (United States); Argonne National Lab. (ANL), Argonne, IL (United States). 10, 2013.
<https://www.osti.gov/biblio/1306469>.
- [2] P. D. Group, P. Zyla, R. Barnett, J. Beringer, O. Dahl, D. Dwyer, D. Groom, C.-J. Lin, K. LUGOVSKY, E. Pianori, et al., “Review of particle physics,” *Prog. Theor. Exp. Phys.* **2020** no. 8, (2020) 083C01.
- [3] L. D. Duffy and K. Van Bibber, “Axions as dark matter particles,” *New J. Phys.* **11** no. 10, (2009) 105008.
- [4] D. J. Marsh, “Axion cosmology,” *Phys. Rept.* **643** (2016) 1–79.
- [5] J. Preskill, M. B. Wise, and F. Wilczek, “Cosmology of the invisible axion,” *Phys. Lett. B* **120** no. 1-3, (1983) 127–132.
- [6] L. F. Abbott and P. Sikivie, “A cosmological bound on the invisible axion,” *Phys. Lett. B* **120** no. 1-3, (1983) 133–136.
- [7] M. Dine and W. Fischler, “The not-so-harmless axion,” *Phys. Lett. B* **120** no. 1-3, (1983) 137–141.
- [8] R. D. Peccei and H. R. Quinn, “CP conservation in the presence of instantons,” *Phys. Rev. Lett.* **38** no. 25, (1977) 1440–1443.
- [9] S. Weinberg, “A new light boson?,” *Phys. Rev. Lett.* **40** no. 4, (1978) 223–226.
- [10] F. Wilczek, “Problem of strong P and T invariance in the presence of instantons,” *Phys. Rev. Lett.* **40** no. 5, (1978) 279–282.
- [11] C. Vafa and E. Witten, “Parity conservation in quantum chromodynamics,” *Phys. Rev. Lett.* **53** no. 6, (1984) 535–536.
- [12] R. Golub and S. K. Lamoreaux, “Neutron electric-dipole moment, ultracold neutrons and polarized ^3He ,” *Phys. Rept.* **237** no. 1, (1994) 1–62.
- [13] G. G. Raffelt, “Astrophysical methods to constrain axions and other novel particle phenomena,” *Phys. Rept.* **198** no. 1-2, (1990) 1–113.
- [14] P. W. Graham, I. G. Irastorza, S. K. Lamoreaux, A. Lindner, and K. A. van Bibber, “Experimental searches for the axion and axion-like particles,” *Annu. Rev. Nucl. Part. Sci.* **65** (2015) 485–514.
- [15] M. Safronova, D. Budker, D. DeMille, D. F. J. Kimball, A. Derevianko, and C. W. Clark, “Search for new physics with atoms and molecules,” *Rev. Mod. Phys.* **90** no. 2, (2018) 025008.

- [16] T. Wu, J. W. Blanchard, G. P. Centers, N. L. Figueroa, A. Garcon, P. W. Graham, D. F. J. Kimball, S. Rajendran, Y. V. Stadnik, A. O. Sushkov, et al., “Search for axionlike dark matter with a liquid-state nuclear spin comagnetometer,” *Phys. Rev. Lett.* **122** no. 19, (2019) 191302.
- [17] I. M. Bloch, R. Shaham, Y. Hochberg, E. Kuflik, T. Volansky, and O. Katz, “Constraints on axion-like dark matter from a SERF comagnetometer,” *Nat. Commun.* **14** no. 1, (2023) 5784.
- [18] J. Lee, M. Lisanti, W. A. Terrano, and M. Romalis, “Laboratory constraints on the neutron-spin coupling of feV-scale axions,” *Phys. Rev. X* **13** no. 1, (2023) 011050.
- [19] D. Gavilan-Martin, G. Lukaszewicz, M. Padniuk, E. Klinger, M. Smolis, N. L. Figueroa, D. F. J. Kimball, A. O. Sushkov, S. Pustelny, D. Budker, et al., “Searching for dark matter with a 1000 km baseline interferometer,” *arXiv preprint arXiv:2408.02668* (2024).
- [20] M. Jiang, H. Su, A. Garcon, X. Peng, and D. Budker, “Search for axion-like dark matter with spin-based amplifiers,” *Nat. Phys.* **17** no. 12, (2021) 1402–1407.
- [21] Z. Xu, X. Ma, K. Wei, Y. He, X. Heng, X. Huang, T. Ai, J. Liao, W. Ji, J. Liu, et al., “Constraining ultralight dark matter through an accelerated resonant search,” *Commun. Phys.* **7** no. 1, (2024) 226.
- [22] T. Kornack and M. Romalis, “Dynamics of two overlapping spin ensembles interacting by spin exchange,” *Phys. Rev. Lett.* **89** no. 25, (2002) 253002.
- [23] E. Babcock, I. Nelson, S. Kadlecik, B. Driehuys, L. Anderson, F. W. Hersman, and T. G. Walker, “Hybrid spin-exchange optical pumping of ^3He ,” *Phys. Rev. Lett.* **91** no. 12, (2003) 123003.
- [24] K. Wei, W. Ji, C. Fu, A. Wickenbrock, V. V. Flambaum, J. Fang, and D. Budker, “Constraints on exotic spin-velocity-dependent interactions,” *Nat. Commun.* **13** no. 1, (2022) 7387.
- [25] K. Wei, T. Zhao, X. Fang, Z. Xu, C. Liu, Q. Cao, A. Wickenbrock, Y. Hu, W. Ji, and D. Budker, “Ultrasensitive atomic comagnetometer with enhanced nuclear spin coherence,” *Phys. Rev. Lett.* **130** no. 6, (2023) 063201.
- [26] R. Shaham, O. Katz, and O. Firstenberg, “Strong coupling of alkali-metal spins to noble-gas spins with an hour-long coherence time,” *Nat. Phys.* **18** no. 5, (2022) 506–510.
- [27] Z. Xu, K. Wei, X. Heng, X. Huang, and Y. Zhai, “Critical dynamics of strongly interacting ensembles in spin-exchange-relaxation-free comagnetometers,” *Phys. Rev. Appl.* **18** no. 4, (2022) 044049.
- [28] T. Kornack, S. Smullin, S.-K. Lee, and M. Romalis, “A low-noise ferrite magnetic shield,” *Appl. Phys. Lett.* **90** no. 22, (2007) 223501.
- [29] T. Kornack, R. Ghosh, and M. Romalis, “Nuclear spin gyroscope based on an atomic comagnetometer,” *Phys. Rev. Lett.* **95** no. 23, (2005) 230801.
- [30] J. Bovy, D. W. Hogg, and H.-W. Rix, “Galactic masers and the Milky Way circular velocity,” *Astrophys. J.* **704** no. 2, (2009) 1704–1709.
- [31] P. F. de Salas and A. Widmark, “Dark matter local density determination: recent observations and future prospects,” *Rep. Prog. Phys.* **84** no. 10, (2021) 104901.
- [32] A. Banerjee, D. Budker, J. Eby, V. V. Flambaum, H. Kim, O. Matsedonskyi, and G. Perez, “Searching for Earth/Solar axion halos,” *J. High Energ. Phys.* **2020** no. 9, (2020) 1–26.
- [33] J. W. Foster, N. L. Rodd, and B. R. Safdi, “Revealing the dark matter halo with axion direct detection,” *Phys. Rev. D* **97** no. 12, (2018) 123006.
- [34] G. P. Centers, J. W. Blanchard, J. Conrad, N. L. Figueroa, A. Garcon, A. V. Gramolin, D. F. J. Kimball, M. Lawson, B. Pelssers, J. A. Smiga, et al., “Stochastic fluctuations of bosonic dark matter,” *Nat. Commun.* **12** no. 1, (2021) 7321.
- [35] M. Lisanti, M. Moschella, and W. Terrano, “Stochastic properties of ultralight scalar field gradients,” *Phys. Rev. D* **104** no. 5, (2021) 055037.
- [36] A. V. Gramolin, A. Wickenbrock, D. Aybas, H. Bekker, D. Budker, G. P. Centers, N. L. Figueroa, D. F. J. Kimball, and A. O. Sushkov, “Spectral signatures of axionlike dark matter,” *Phys. Rev. D* **105** no. 3, (2022) 035029.
- [37] A. Derevianko, “Detecting dark-matter waves with a network of precision-measurement tools,” *Phys. Rev. A* **97** no. 4, (2018) 042506.
- [38] “The axion-nucleon coupling limits for ChangeE,” 2023. <https://github.com/JiaLiu2023/Axion-data>.
- [39] I. M. Bloch, G. Ronen, R. Shaham, O. Katz, T. Volansky, and O. Katz, “New constraints on axion-like dark matter using a Floquet quantum detector,” *Sci. Adv.* **8** no. 5, (2022) eabl8919.
- [40] C. Abel, N. J. Ayres, G. Ban, G. Bison, K. Bodek, V. Bondar, E. Chaneel, C. Crawford, M. Daum, B. Dechenaux, et al., “Search for ultralight axion dark matter in a side-band analysis of a ^{199}Hg free-spin precession signal,” *SciPost Phys.* **15** (2023) 058.
- [41] M. Buschmann, C. Dessert, J. W. Foster, A. J. Long, and B. R. Safdi, “Upper limit on the QCD axion mass from isolated neutron star cooling,” *Phys. Rev. Lett.* **128** no. 9, (2022) 091102.
- [42] P. Carena, T. Fischer, M. Giannotti, G. Guo, G. Martínez-Pinedo, and A. Mirizzi, “Improved axion emissivity from a supernova via nucleon-nucleon bremsstrahlung,” *J. Cosmol. Astropart. Phys.* **2019** no. 10, (2019) 016.
- [43] A. Bhusal, N. Houston, and T. Li, “Searching for solar axions using data from the sudbury neutrino observatory,” *Phys. Rev. Lett.* **126** no. 9, (2021) 091601.
- [44] M. V. Beznogov, E. Rrapaj, D. Page, and S. Reddy, “Constraints on axion-like particles and nucleon pairing in dense matter from the hot neutron star in HESS J1731-347,” *Phys. Rev. C* **98** no. 3, (2018) 035802.
- [45] L. Di Luzio, M. Fedele, M. Giannotti, F. Mescia, and E. Nardi, “Stellar evolution confronts axion models,” *J. Cosmol. Astropart. Phys.* **2022** no. 02, (2022) 035.
- [46] J. H. Chang, R. Essig, and S. D. McDermott, “Supernova 1987A constraints on sub-GeV dark sectors, millicharged particles, the QCD axion, and an axion-like particle,” *J. High Energ. Phys.* **2018** no. 09, (2018) 1–45.
- [47] N. Bar, K. Blum, and G. D’Amico, “Is there a supernova bound on axions?,” *Phys. Rev. D* **101** no. 12, (2020) 123025.
- [48] S. Afach, D. Aybas Tumturk, H. Bekker, B. C. Buchler, D. Budker, K. Cervantes, A. Derevianko, J. Eby, N. L. Figueroa, R. Folman, et al., “What can a gnome do? search targets for the global network of optical magnetometers for exotic physics searches,” *Ann. Phys.* **536** no. 1, (2024) 2300083.
- [49] H. Masia-Roig, N. L. Figueroa, A. Bordon, J. A. Smiga, D. Budker, G. P. Centers, A. V. Gramolin, P. S. Hamilton, S. Khamis, C. A. Palm, et al., “Intensity interferometry for ultralight bosonic dark matter detection,” *Phys. Rev. D* **108** no. 1, (2023) 015003.
- [50] E. Boto, N. Holmes, J. Leggett, G. Roberts, V. Shah, S. S. Meyer, L. D. Muñoz, K. J. Mullinger, T. M. Tierney, S. Bestmann, et al., “Moving magnetoencephalography towards real-world applications with a wearable system,”

- [Nature](#) **555** no. 7698, (2018) 657–661.
- [51] L. Tauxe, [Essentials of paleomagnetism](#). Univ of California Press, 2010.
- [52] B. Lancor and T. G. Walker, “Polarization limits in K-Rb spin-exchange mixtures,” [Phys. Rev. A: At., Mol., Opt. Phys.](#) **83** no. 6, (2011) 065401.
- [53] B. A. Brown, G. F. Bertsch, L. M. Robledo, M. V. Romalis, and V. Zelevinsky, “Nuclear matrix elements for tests of local Lorentz invariance violation,” [Phys. Rev. Lett.](#) **119** no. 19, (2017) 192504.
- [54] A. Almasi, J. Lee, H. Winarto, M. Smiciklas, and M. V. Romalis, “New limits on anomalous spin-spin interactions,” [Phys. Rev. Lett.](#) **125** no. 20, (2020) 201802.
- [55] G. Vasilakis, J. M. Brown, T. W. Kornack, and M. V. Romalis, “Limits on new long range nuclear spin-dependent forces set with a $K\text{-}^3\text{He}$ co-magnetometer,” [Phys. Rev. Lett.](#) **103** (2009) 261801.
- [56] J. M. Brown, S. J. Smullin, T. W. Kornack, and M. V. Romalis, “New limit on Lorentz and CPT-violating neutron spin interactions,” [Phys. Rev. Lett.](#) **105** (2010) 151604.
- [57] S. F. Potter, N. A. Gumerov, and R. Duraiswami, “Fast interpolation of bandlimited functions,” in [2017 IEEE International Conference on Acoustics, Speech and Signal Processing \(ICASSP\)](#), pp. 4516–4520. 2017.
- [58] A. Dutt and V. Rokhlin, “Fast Fourier transforms for nonequispaced data,” [SIAM J. Sci. Comput.](#) **14** no. 6, (1993) 1368–1393.
- [59] C. Munteanu, C. Negrea, M. Echim, and K. Mursula, “Effect of data gaps: Comparison of different spectral analysis methods,” [Ann. Geophys.](#) **34** no. 4, (2016) 437–449.
- [60] W. Terrano and M. Romalis, “Comagnetometer probes of dark matter and new physics,” [Quantum Sci. Technol.](#) **7** no. 1, (2022) 014001.
- [61] I. M. Bloch, Y. Hochberg, E. Kuflik, and T. Volansky, “Axion-like relics: New constraints from old comagnetometer data,” [J. High Energ. Phys.](#) **2020** no. 1, (2020) 1–38.
- [62] K. A. Olive and M. Pospelov, “Environmental dependence of masses and coupling constants,” [Phys. Rev. D](#) **77** (2008) 043524.
- [63] M. Pospelov, S. Pustelny, M. P. Ledbetter, D. F. Jackson Kimball, W. Gawlik, and D. Budker, “Detecting domain walls of axionlike models using terrestrial experiments,” [Phys. Rev. Lett.](#) **110** no. 2, (2013) 021803.
- [64] G. Cowan, K. Cranmer, E. Gross, and O. Vitells, “Asymptotic formulae for likelihood-based tests of new physics,” [Eur. Phys. J. C](#) **71** (2011) 1554. [Erratum: [Eur.Phys.J.C](#) 73, 2501 (2013)].